Complex kinematic rupture of the Mw 5.9, 1999 Athens earthquake as revealed by the joint inversion of regional seismological and SAR data

D. Baumont,[1] O. Scotti,[1] F. Courboulex[2] and N. Melis[3]

[1] *IRSN/DEI/SARG/BERSSIN,* 60-68 *Av. du Général Leclerc,* PO Box 17, *Fontenay aux Roses* 92262, *France. E-mail: david.baumont@irsn.fr*
[2] *Géosciences Azur,* 250 *Av. Albert Einstein, Valbonne* 06560, *France*
[3] *NOA-IG,* PO Box 20048, *Lofos Nymfon, Athens* GR-118 10, *Greece*

SUMMARY

Slip distributions of the moderate magnitude (Mw 5.9), 1999 Athens earthquake, inverted from surface waves and interferometric Synthetic Aperture Radar (SAR) images, show very different characteristics. The robustness analysis proposed in this study, confirms the discrepancy between the well-constrained features of each individual solution. Irrespective of the hypotheses we made (data/modeling errors, slow deformation, post- or pre-seismic slip), the joint inversion of the two data sets led to a complex and heterogeneous rupture model. This model is characterized by a short rise time (<5 s) slip patch centred on the hypocentre, extending bilaterally up to 4 km depth and down to 17 km and releasing approximately 70 per cent of the total moment. Located further to the WNW and releasing the remaining 30 per cent of the total moment, a long rise time slip patch extends from 8 to 17 km depth. If the short rise time slip patch propagated above and below the brittle zone delineated by the aftershocks, the long rise time slip patch (slow deformation) appears to be mostly confined below the brittle zone. This unified model satisfies the analysis of the seismic and geodetic slip distributions as well as the location of the aftershock sequence and attests to the diversity of the crustal response even for moderate size faults.

Key words: complex slip distribution, joint inversion, moderate magnitude earthquake, slow deformation.

1 INTRODUCTION

On 1999 September 7, a moderate magnitude (Mw 5.9), crustal earthquake occurred less than 10 km to the west of the metropolitan area of Athens (Fig. 1). Despite its moderate size, this earthquake caused extensive damage in Athens and its surroundings, especially in the northern and western suburbs where the macroseismic intensities reached IX locally (Anastasiadis *et al.* 1999). Some 100 buildings collapsed (among which were reinforced concrete buildings) and more than 10 000 buildings were declared to be either heavily damaged or damaged beyond repair. One hundred and forty-three people died and approximately 100 000 people were homeless during the first days following the earthquake.

Moderate magnitude earthquakes occurring at close distances to a densely populated area or a strategic installation represent the typical seismic hazard in Europe and yet little is known about their rupture process and kinematic characteristics compared to large earthquakes. Indeed, moderate earthquakes have a rich frequency content, which is difficult to model, and are usually poorly recorded. In this respect, the Athens earthquake is exceptional: (i) the main shock and the largest aftershocks were recorded by a remarkably good azimuthal coverage of regional broad-band stations (Stavrakakis *et al.*

2002) and (ii) numerous SAR images were available. On the one hand, several rupture models were proposed for the Athens earthquake based on the analysis of regional broad-band data using an empirical Green function (EGF) approach. By forward modelling, Tselentis & Zahradnik (2000b) proposed a 10-km asperity rupture model. Baumont *et al.* (2002) and Roumelioti *et al.* (2003) inverted the apparent source time functions (ASTFs) for a more detailed rupture model (Fig. 2), showing a bilaterally upward and downward propagating rupture of roughly similar amplitude and extent. Only the details of the slip distributions are different as a result of differences in the calculated ASTFs and in the modelling parametrization. On the other hand, Kontoes *et al.* (2000) computed several SAR interferometric deformation field images, showing two asymmetric fringes. To satisfactorily model this asymmetry, the authors appealed to two distinct, non-coplanar, N116°, 54° south dipping faults with homogeneous slip. According to their model, the total moment released is of the order of 1.5×10^{18}N m, which is 30–50 per cent larger than the seismic moment estimates (Table 1). Compared to the seismic rupture models, this model is suggesting the existence of a larger amount of slip at depth.

In this paper, we test whether the discrepancy between seismic and geodetic models could be explained by data and modelling errors
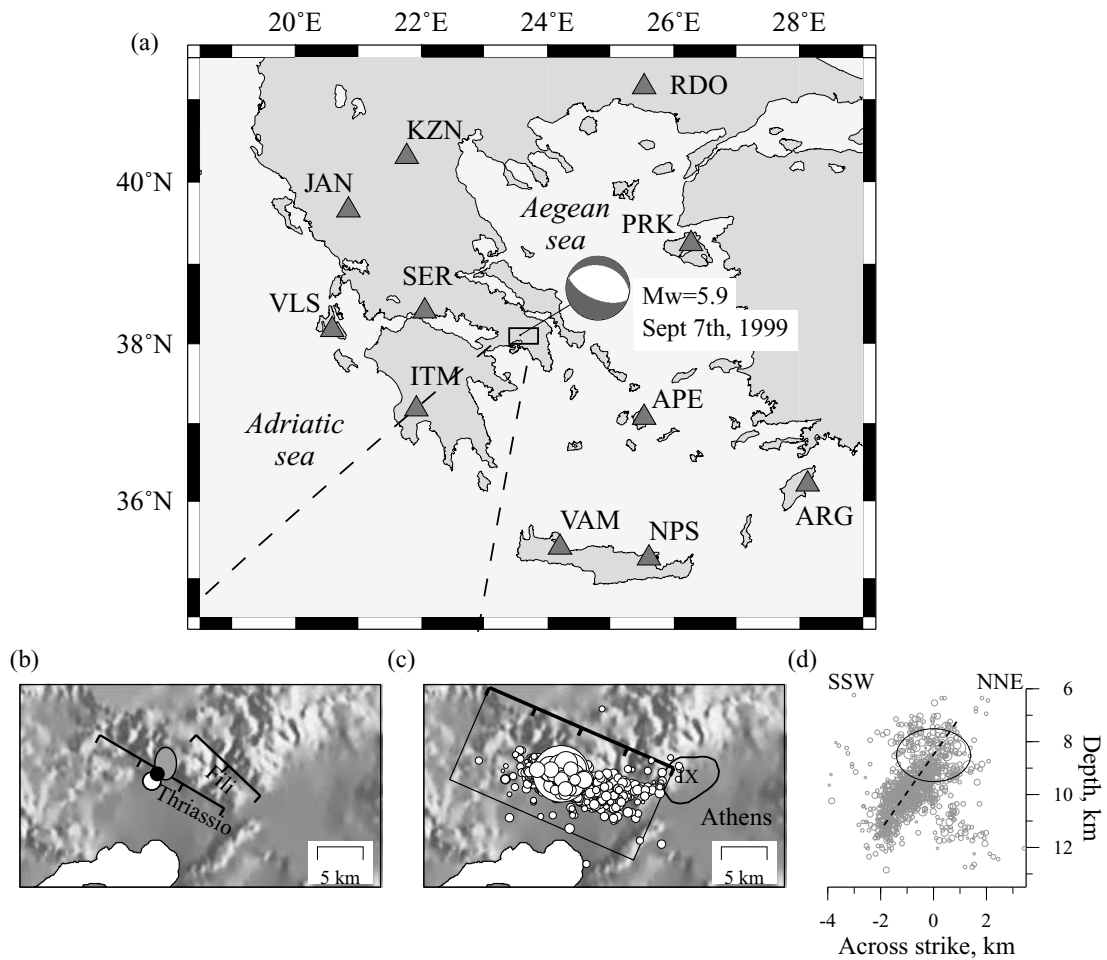
Figure 1. (a) Map of regional broad-band stations used in this study (triangles) showing their optimal distribution with respect to the epicentre of the Athens 1999 earthquake. The National Observatory of Athens operates these stations with the exception of Sergoula (SER), which is operated by Patras and Prague universities. The focal mechanism calculated by Zahradnik (2002) shows an almost east–west oriented normal fault. (b) Epicentre location proposed by Papadimitriou *et al.* (2000) (white ellipse) and by the International Seismological Centre (grey ellipse) relative to the Thriassio and Fili faults (black lines). The epicentral location of the initial model is also shown in black (Table 1). (c) Initial fault model used in this study relative to our best relocated aftershocks. These aftershocks, recorded by a temporary network (run by the NOA between 1999 September 13 and November 11), were relocated using a Joint Hypocentre Determination procedure (Pujol 1988). (d) Our best relocated events highlight a 55°, south dipping fault plane.
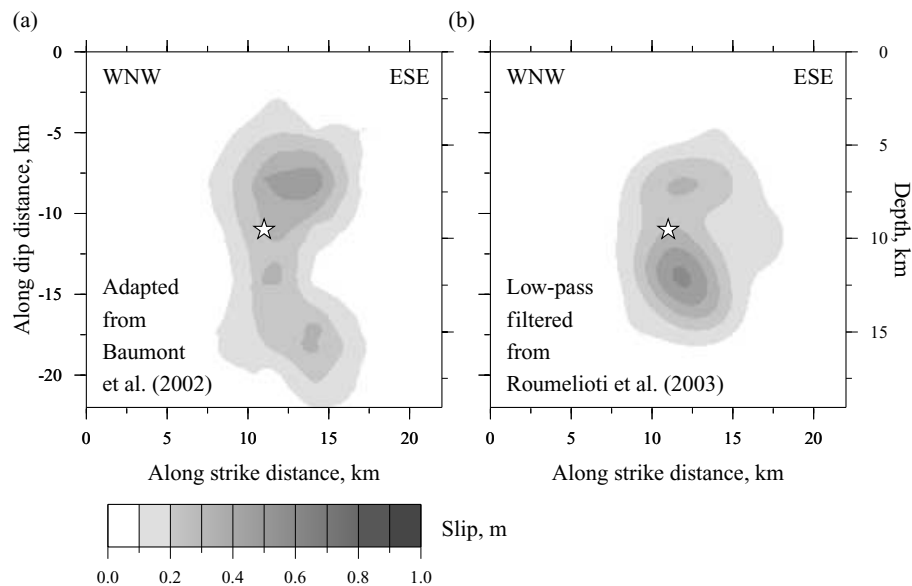
Figure 2. Comparison between the slip distributions obtained by (a) Baumont *et al.* (2002) and (b) Roumelioti *et al.* (2003).

Table 1. Locations, focal mechanisms and seismic moment of the 1999 Athens earthquake reported by different institutes or authors.

Longitude (°)	Latitude (°)	Depth (km)	Strike (°)	Dip (°)	Rake (°)	Mo (10^{18}N m)	Institute or authors
23.58	38.08	16.8	113	39	−90		Papadopoulos *et al.* (2000)
23.582	38.122	9.4					ISC bulletin
23.605	38.119	8.0	136	56	−82	0.9	USGS-NEIC
23.565	38.105	8	105	55	−80	1.0	Papadimitriou *et al.* (2000)
23.640	37.870	15.00	116	39	−81	1.1	HRVD-CMT
23.54	38.06	10	115	57	−80	0.9	Louvari & Kiratzi (2001)
		10	115	60	−80	0.6	Sargeant *et al.* (2002)
			112	61	−84		Zahradnik (2002)
			117	52			Tselentis & Zahradnik (2000a)

USGS-NEIC is U.S Geological Survey, National Earthquake Information Center.

Table 2. Parameter space explored in this study and optimal values inverted or fixed (shaded) corresponding to the results presented in Figs 2, 4 and 6.

		Parameter space	Fig. 2	Fig. 4	Fig. 6
Hypocentre	Longitude	23.572° ± 3 km	23.572°	23.584°	23.582°
	Latitude	38.112° ± 3 km	38.112°	38.124°	38.122°
	Depth (km)	8 to 16	9.5	9.6	9.5
Geometry	L × W (km²)	22 × 18, 22 × 22, 35 × 22	118	138	148
	Strike (°)/dip (°)	112/40, 50, 60		112/60	
	Rake (°)	−84; −110 to −70		−84	
Rupture model	Corr. length (km)	4 or 10	4	10	4
	Slip (m)	0 to 1	0.29	0.43	0.36
	Rise (s)	0 to 5	1.4	–	1.8
	Vr (km s^{-1})	2.5 to 3.2	2.9	–	2.9
	M_0 (10^{18} N m)	–	1.1	1.8	1.6
	Stress drop (MPa)	–	2	3	2
	rms$_{ASTFs}$ (10^6 N m s^{-1})	–	1.6	–	2.2
	rms$_{SAR}$ (mm)	–	–	6.1	8.2

and propose a robustness scheme to outline the well-constrained features of each individual solution. The different hypotheses tested through a joint inversion allow us to propose a new rupture model for the Athens earthquake that satisfactorily predicts both the geodetic and seismic data.

2 FAULT PARAMETRIZATION

Published earthquake parameters are listed in Table 1. Our fault model (Table 2) is composed of a single plane centred on the hypocentre. Among the various published solutions, we chose epicentral locations within the solutions of Papadimitriou *et al.* (2000) and the International Seismological Centre (ISC; Fig. 1b) and tested for a hypocentral depth between 8 and 17 km. The fault dimensions were chosen to include all the previous estimates of rupture area: 20 × 16 km² based on the aftershock distribution (Tselentis & Zahradnik 2000b), 10 × 11 km² by inverting SAR data (Kontoes *et al.* 2000), 18 × 10 km² by modelling far field body waves (Louvari & Kiratzi 2001), and 10 × 15 km² by inverting the ASTFs (Baumont *et al.* 2002; Roumelioti *et al.* 2003).

Two 110–130°N, south dipping normal faults are clearly expressed on the morphology of the epicentral area, the Fili and Thriassio faults, however, the field investigation did not allow a direct identification of the activated fault, since no extended surface rupture was observed (Pavlides *et al.* 2002). According to published aftershock distributions and focal mechanism solutions, the rupture

occurred on a 110–140°N, 40–60° dipping normal fault. Following the focal mechanism solution proposed by Zahradnik (2002) and our aftershock distribution (Fig. 1d), the fault strike and dip angles were fixed at 112° and 60°, respectively. Alternative fault geometries were tested and did not affect the main characteristics of either the geodetic or the seismic rupture models. The rake was fixed to −84°. The fault model was subdivided using a regular grid mesh of 3 by 3 km². For each sub-fault, we define a physically reasonable range of values for the slip amplitude, the rupture and the rise time. Two correlation lengths were tested. The seismic moment used to normalize the ASTFs was fixed at 1.1 × 10^{18} N m.

3 IMPACT OF SURFACE-WAVE MODELLING ON THE SEISMIC RUPTURE MODEL

In our previous study (Baumont *et al.* 2002), we did not take into account the sensitivity of surface-waves to the assumed source depth, which may modify the slip distribution and may reduce the discrepancy between the geodetic and seismic slip models. In order to estimate a surface-wave depth correction, we assume that surface-wave records can be modelled by summing the first three modes. Using the regional velocity model proposed by Tselentis & Zahradnik (2000b), we model the seismograms up to 2 Hz through a mode summation approach (Herrmann 2002). We consider a source-station distance of 200 km, and perform several computations with a source located

at different depths between 2 and 20 km. The resulting relative amplitude change of the surface waves as a function of the source depth is used to model the ASTFs more correctly.

ASTFs were retrieved from the most energetic phases, i.e. the Rayleigh and Love waves, filtered (0.08–10 Hz) to insure a good signal-to-noise ratio. We applied a time-domain iterative deconvolution with positivity constraints. To get rid of the frequencies higher than the EGF corner frequency, a Gaussian filter (2 Hz) was applied.

Three EGFs were considered to evaluate the ASTFs and their uncertainties. ASTFs were inverted for the kinematic rupture model using a damped-least square scheme with inequality constraints accounting for our surface-wave depth correction. The ASTF uncertainties were introduced through a covariance matrix on data reduced to its diagonal elements. We fixed the hypocentre at 9.5 km depth close to the ISC determination (Table 1). Fig. 3 shows one of our best inversion solutions using this new ASTF modelling. This rupture
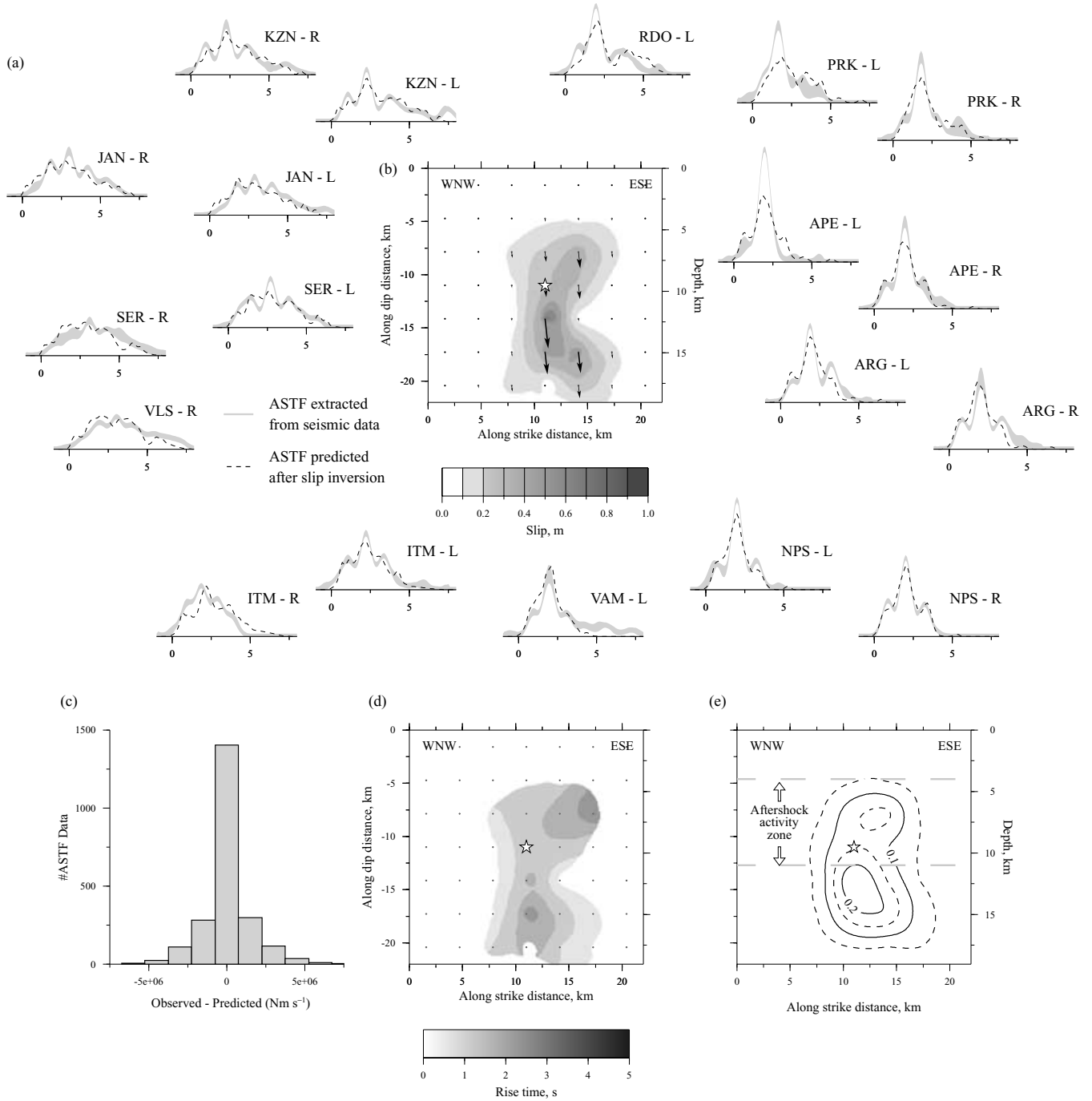
Figure 3. Best kinematic rupture model for the Athens earthquake inverted from Rayleigh (R) and Love (L) waves assuming a surface wave depth correction (see text). (a) Azimuthal variations of ASTFs (after Baumont *et al.* 2002) and associated uncertainties (shaded grey areas). The ASTFs were normalized using the seismic moment of the Harvard CMT Catalog (HRVD-CMT) solution (Table 1). (b) Slip and (d) rise time distributions inverted from the ASTFs data assuming the fault geometry shown in Fig. 1c (see Table 2). This rupture model predicts satisfactorily the ASTFs (dashed lines in a) with (c) an rms of 1.6×10^6 N m s^{-1}. Notice that rms was normalized by the shear modulus value (3×10^{10} N m^{-2}). (e) Robustness analysis highlighting the coherent features (see text). The aftershock activity zone (Voulgaris *et al.* 2000) suggests that the rupture propagated below the base of the brittle zone.

model satisfactorily predicts both the amplitudes and timing of the peaks observed in the ASTFs, with an rms of 1.6×10^6 N m s^{-1} (Figs 3a and c). The rupture is characterized by a bilateral upward and downward propagation covering 120 km^2 (Fig. 3b). Although the mean slip amplitude is equal to approximately 30 cm, the slip is heterogeneous, reaching 60 cm locally in the deeper part of the fault. The rupture velocities average around 2.9 km s^{-1}, but are poorly constrained. Rise time values (Fig. 3d) vary between 0.5 and 2.5 s. In this model the rupture lasts roughly 5 s.

Thus, accounting for the surface wave sensitivity to depth results in an overall transfer of slip (of the order of 20 per cent) from the shallowest part of the fault to the deeper part (*cf.* Figs 2a and 3b), but does not affect the geometry of our slipping patch.

4 IMPACT OF ASTF ERRORS ON THE SEISMIC RUPTURE MODEL

As previously mentioned, three EGFs were considered to estimate the ASTFs and their uncertainty. Nonetheless, these uncertainties do not cover the differences between our ASTFs and those obtained by Roumelioti *et al.* (2003). In order to further qualify the robustness of the main features of our seismic slip solution, we performed a stochastic exploration of the model space and retained all models with an rms value as large as 2×10^6 N m s^{-1}. Starting from our best solution, which has an rms of 1.6×10^6 N m s^{-1}, a set of models was generated by random perturbation. At each iteration, the random model is allowed to change up to 2 cm for the slip amplitude and up to 0.1 s for rupture time and rise time. The new model is retained if it satisfactorily reproduces the ASTFs. The parameter space is then re-explored (30 000 times) starting from the most updated model and only 600 are retained. Because strike and dip angles have only a minor effect on the solution, they were kept fixed. The hypocentral depth was also kept fixed considering the narrow range of the best determinations (8 to 10 km).

To highlight the coherent features of the slip distributions, the 600 models are low-pass filtered (10-km-cut-off wavelength) and the lowest slip value is reported at each grid point (Fig. 3e). As testified by this robustness analysis, the main characteristics of the slip distribution (the extension of the fault and the presence of two slipping patches vertically aligned on either side of the hypocentre) are well constrained.

It is interesting to compare the repartition of the slip with the aftershocks because they may help delimit the base of the brittle zone. Indeed, the aftershock sequence recorded by the NOA temporary network outlines a 15-km-long region between 6 and 12 km depth (Figs 1c and d). The complete data set published by Papadimitriou *et al.* (2002) and Voulgaris *et al.* (2000) shows more activity to the west but remains mostly confined above 11 km depth. The rupture may have thus propagated below the brittle zone (Fig. 3e).

5 SINGLE FAULT, GEODETIC RUPTURE MODELS

As previously explained, Kontoes *et al.* (2000) appealed to two distinct, non-coplanar, 116°N, 54° south dipping faults with homogeneous slip to model the asymmetry of the surface deformation field. Because the seismological data cannot confirm or exclude the activation of a second fault plane, we prefer to address the question of whether a single heterogeneous fault segment could equally well satisfy the asymmetric deformation field.

The observed deformation field (Fig. 4a) is regularly sampled (36 points). We can rule out any significant potential biases in the

deformation data as a result of troposphere perturbations. Indeed, Kontoes *et al.* (2000) showed in their analysis that an additional SAR interferogram covering a different time period [1997 November 27 to 1999 September 23] led to a very similar image. Data errors were deduced from the comparison of these two interferograms and fixed to 4 mm for the inner fringes and to 8 mm for the ill-defined fringe of zero deformation. The uncertainties on the SAR data were introduced through a covariance matrix on data reduced to its diagonal elements. However, because the least-squares criteria can be sensitive to a very small number of data with large errors, low weights were applied to data with large deviations from the values predicted by the current model. The deformation field is modelled using the analytical solution of Okada (1992) in a homogeneous, elastic, half-space. Because slip models inverted from geodetic data are sensitive to the fault location, we invert for both the slip distribution and the hypocentre location (within the *a priori* uncertainty; Table 2) through an iterative weighted least-squares scheme with inequality constraints (Menke 1984). As a reminder the fault model is centred on the hypocentre.

Fig. 4(d) shows our best slip model as well as the predicted and observed SAR interferograms covering the period [1998 September 19 to 1999 October 9]. The synthetic interferogram (Fig. 4b) reproduces well the inner fringes, but not the poorly defined zero-deformation fringe. Our best geodetic slip model exhibits features that are significantly different from the seismological solutions (Figs 2 and 3): a main slip patch located in the WNW deep part of the fault (mean amplitude equal to 45 cm) and a minor one in its ESE shallow part (mean amplitude equal to 20 cm). This model is overall very similar to the one proposed by Kontoes *et al.* (2000) in the sense that the two slipping patches/dislocations inverted have comparable spatial dimensions and amplitudes. The moment released was estimated at approximately 1.8×10^{18} N m (Table 2), which is close to the estimation of Kontoes *et al.* (2000), but larger than the seismic moment estimations (Table 1). The fault location we inverted is within the error bars of the ISC determination, while its depth remained unchanged. These results are not affected by the initial hypocentral location tested between 8 and 17 km. The fault trace projection lies on the NW extension of the Fili fault.

Several other inversions were made:

(i) considering only the 28- and 56-mm fringes;

(ii) considering the other available interferogram (Kontoes *et al.* 2000);

(iii) allowing the rake to vary smoothly between $-110°$ and $-70°$ (which allowed a better modelling of the zero-deformation fringe).

Nevertheless, the main characteristics of the geodetic slip distribution remain. As for the seismological data, the robustness analysis of this solution confirms that the main features of the slip model are well constrained (Fig. 4e) and differ significantly from the ones inverted from seismological data (Fig. 3e).

6 SLIP MODELS FROM THE JOINT INVERSION OF GEODETIC AND SEISMIC DATA

As demonstrated in the previous sections, the seismic and geodetic data produce slip distributions with well-resolved but very different characteristics. Two hypotheses can be proposed to interpret the origin of this discrepancy: (i) data/modelling errors and/or (ii) differences in the bandpass of the two data sets.
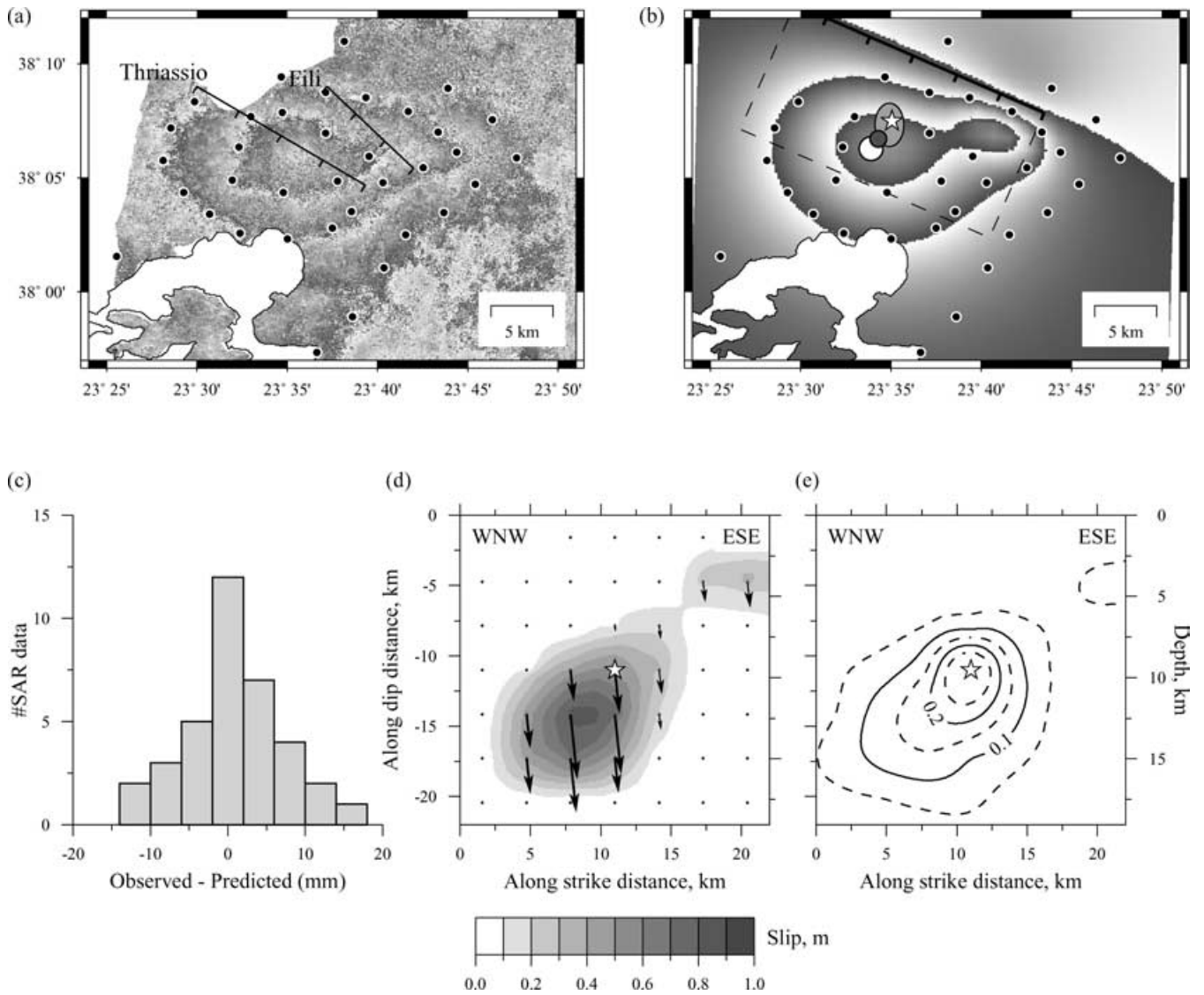
Figure 4. Best rupture model inverted for the Athens earthquake from geodetic data. (a) SAR interferogram spanning the period [1998 September 19 to 1999 October 9] computed by Kontoes *et al.* (2000). (b) The best fault location (star) is within the error bars of the ISC determination (see legend of Fig. 1). The synthetic interferogram reproduces well the inner fringes with (c) an rms around 6 mm. (d) Our best slip model is characterized by a main slip patch located in the WNW deep part of the fault and a minor one in the ESE shallow part. The corresponding moment, 1.8×10^{18} N m, is larger than the seismological estimates (Table 1). (e) Robustness analysis showing that the ESE patch is at the limit of the resolution, whereas the main WNW patch is well constrained.

6.1 Hypothesis 1: data/modelling errors

Assuming that the discrepancy is only the result of data/modelling errors, we perform a joint inversion in order to produce a model that predicts reasonably well both data sets. We adopt the approach proposed by Julià J. *et al.* (2000), in which each data set is equally weighted through an error function, defined as follows:

$$\text{Err} = \left[\frac{(1-p)}{N} \sum_{i=1}^{N} \left(\frac{\delta\text{ASTF}_i - G_{ij}\delta X_j}{\sigma_i} \right)^2 \right.$$
$$\left. + \frac{p}{M} \sum_{i=1}^{M} \left(\frac{\delta\text{SAR}_i - H_{ij}\delta X_j}{\sigma_i} \right)^2 \right]. \quad (1)$$

δASTF and δSAR describe the residual data, G and H the partial derivative matrices and δX the model correction. The partial deriva-

tive matrices were previously defined for the seismological and geodetic data. To equalize the data contribution of each data set and limit physical unit problems, the individual errors are divided by the number of data points (N or M) and by the data variance (σ^2). To modify the relative influence of each data set, a p-weighting factor is introduced in the joint inversion scheme. Fig. 5 shows the degradation of each data set rms with respect to their best individual fit as a function of the p-weighting factor. For $p = 0$, the solution is constrained by the ASTFs, whereas for $p = 1$, the solution is controlled by the SAR data. The model space explored and the inversion scheme are similar to the ones considered in the previous sections. Several inversions were performed testing various hypocentral locations (ATHU, ISC), fault dips (50° to 60°), elastic parameters [$1 - (Vp/Vs)^2 = 0.6$ to 0.7], starting models (homogeneous, pulse, best seismological or geodetic models).
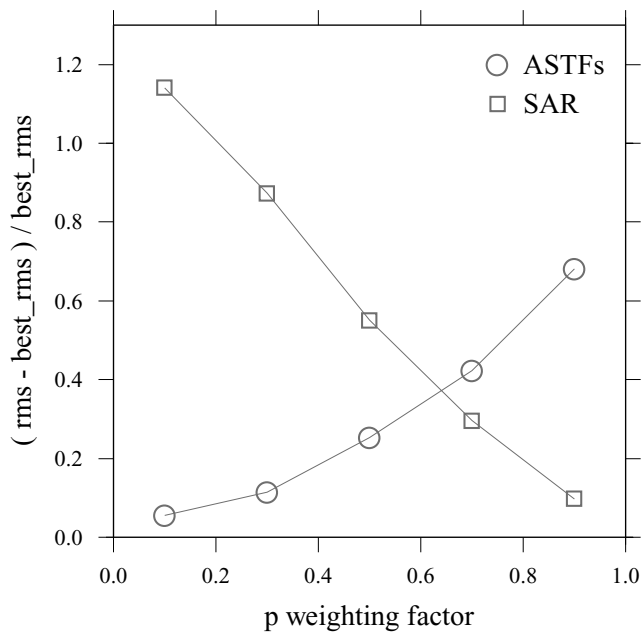
Figure 5. Degradation of each data set rms with respect to their best individual fit as a function of the *p*-weighting factor used in the joint inversion scheme. For $p = 0$, the solution is constrained by the ASTFs, whereas for $p = 1$, the solution is controlled by the SAR data. The choice of *p* is subjective, nonetheless, in this case (Fig. 6), $p = 0.65$ appears as a good compromise.

The best inverted models were found assuming our previous fault geometry (described in Table 2), a starting slip model given by the geodetic solution (Fig. 4) and a $p = 0.65$, which is a good compromise between the two data sets (Fig. 5). As shown in Fig. 6(a), the rupture model satisfactorily predicts the ASTFs, in particular the amplitudes and timing of the observed peaks at the stations located between 45°N and 225°N (PRK, APE, ARG, NPS, VAM and ITM). The predicted ASTFs are nonetheless (i) too long at PRK, APE, ARG and NPS and (ii) too impulsive at JAN, SER and VLS. Concerning the geodetic data, our slip model reproduces well the observed 28-mm fringe and to a lesser extent the 56-mm fringe (Fig. 6f). The resulting slip model (Fig. 6b) shows an overall rupture area (150 km^2) similar to the one delineated by the geodetic solution (Fig. 4). The details of the slip distribution in the central part of the fault are very similar to the seismic solution (Fig. 3). The mean and maximum slip values are equal to approximately 0.4 and 1 m and the estimated stress drop is on the order of 2 MPa. In this model, the average rupture velocity is approximately 2.9 km s^{-1}. The rise time distribution is however very heterogeneous. In the central part of the fault, the rise time is similar to the one previously inverted from seismic data (Fig. 2d), between 0.5 and 2.5 s, whereas in the WNW patch, a long rise time value (close to our 5-s upper limit value) is required.

Compared to the seismic models, the joint models we obtained are characterized by the presence of additional slip patches in the WNW deeper part of the fault and in its ESE shallower part, required to fit the geodetic data (irrespective of the SAR interferogram considered). These patches are not artefacts resulting from an underestimation of the seismic moment used to normalize the ASTFs. Indeed, changing the value of M0 would only result in a homothetic change of the slip distribution inverted from the ASTFs.

6.2 Hypothesis 2: differences in the bandpass of the two data sets

In this hypothesis, we investigate the possibility that the discrepancy between the seismic and geodetic slip models is the result of differences in either the time window over which the observations are made (a few seconds for the seismic data, a few weeks for the geodetic data), or the frequency content of the data (ASTFs are bandpass filtered).

Pre-shock and aftershock activity may have contributed to the deformation registered by the SAR data. However, the regional network recorded little activity before the main shock (Papadopoulos *et al.* 2000), excluding any significant seismic deformation, and the aftershocks were located at shallower depths (Voulgaris *et al.* 2000) than the WNW slip patch. Concerning the ESE additional patch, we cannot exclude an aftershock contribution to this additional slip.

The additional slip patches could also be associated with a slow deformation, too low frequency to be detected in the ASTFs analysis. Following Fig. 6(d), we relaxed the constraint on the rise time and allowed it to vary up to 100 s. The resulting joint solution produces a better fit to the data, equivalent to the individual solutions. We performed a similar robustness analysis on this last joint solution. For each solution retained, we separated the short rise time (<5 s) contributions from the longer ones. As shown in Fig. 7, the well-constrained features of the joint solutions are: (i) a short rise time contribution extending above and below the brittle zone and (ii) a long rise time contribution (slow deformation) corresponding to the additional slip required by the geodetic solution (Fig. 4e) in the WNW deeper part of the fault, located below the brittle zone.

7 DISCUSSION AND CONCLUSIONS

Slip distributions of the moderate magnitude (Mw 5.9), 1999 Athens earthquake inverted from broad-band seismic recordings and from interferometric SAR images have very different characteristics. Through a sensitivity study to the model parameters and a robustness analysis of the solutions, we showed that the main features inverted from each data set alone are well constrained.

Two hypotheses were tested through a joint inversion to explain the origin of this discrepancy: (i) data/modelling errors and (ii) differences in the bandpass of the two data sets. Irrespectively of the hypotheses, the new rupture model that emerges from this study is composed of two well-constrained slip patches with different rise times. The short rise time (approximately 1–2 s) patch is centred on the hypocentre and released approximately 70 per cent of the total moment. Interestingly, the rupture propagated bilaterally above and below the brittle zone as delimited by the aftershock activity. The remaining 30 per cent of the total moment was released further to the WNW, through a slow deformation process confined below the brittle zone.

Slow deformation processes have been reported at depth following large earthquakes along subduction zones (e.g. Bürgmann R. *et al.* 2001; Ruegg *et al.* 2001; Yagi *et al.* 2001) and along strike-slip plate boundaries (Ergintav *et al.* 2002; Bürgmann R. *et al.* 2003). Recent data have also documented the occurrence of seismically induced deformation in the upper few kilometers of the crust along secondary faults (Fialko *et al.* 2002). Although in the case of the Athens earthquake, it is not possible to conclude the timing of this slow deformation (pre-seismic, coseismic, or post-seismic), the analysis of the seismic and geodetic slip distributions combined with the
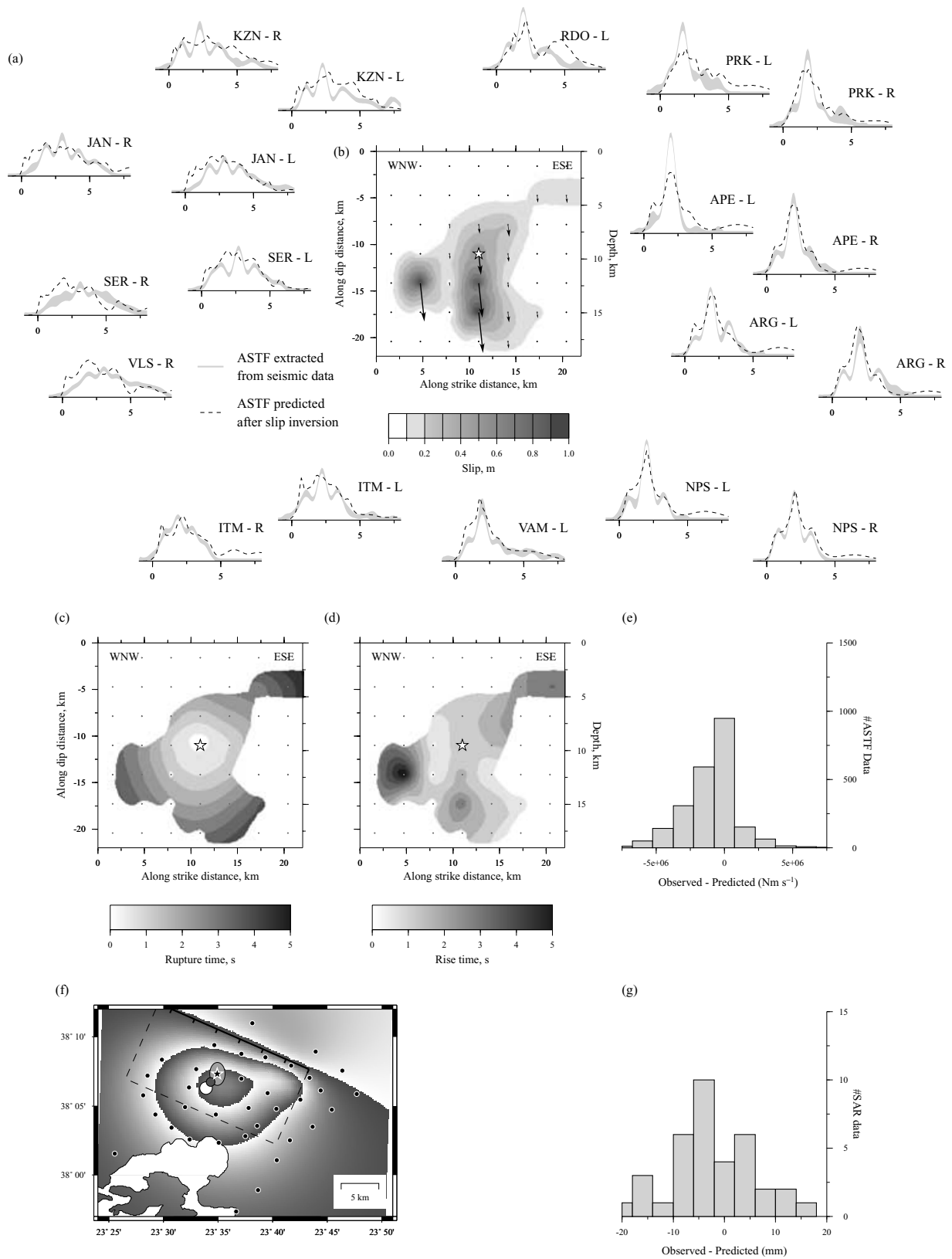
Figure 6. Best rupture model jointly inverted from seismic and geodetic data ($p = 0.65$) assuming only data/modeling errors (see text). We fixed the hypocentre after the ISC location (Table 2) and used the best geodetic solution as a starting model. (b) The slip distribution exhibits additional slip patches to the WNW and ESE compared with the seismic slip model (Fig. 3b). (c) The rupture is quasi-circular with an average rupture velocity of 2.9 km s^{-1}. (d) The rise time distribution is rather heterogeneous and covers the space model (Table 2). Notice the long rise time required by the WNW slip patch. (a) The predictions (dashed lines) of the ASTFs are slightly degraded for eastern and western stations compared to those obtained in Fig. 3, as well as (f) the predicted interferogram compared to Fig. 4, as shown by (e, g) skewed misfit distributions (ASTFs rms = 2.2×10^6 N m s^{-1}, SAR rms = 8.2 mm).
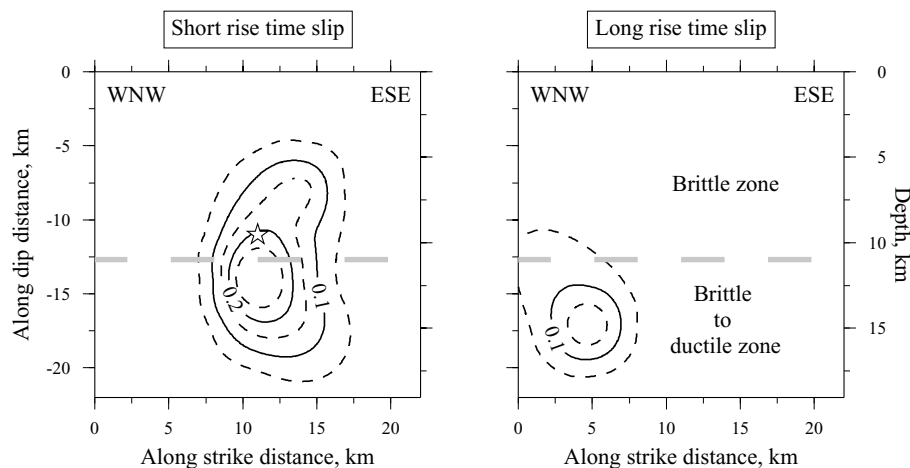
Figure 7. Well-constrained features of our best joint solution allowing for slow deformation (see text). This robustness analysis is based on a stochastic exploration retaining all models with $rms_{SAR} < 9$ mm and $rms_{ASTFs} < 2 \times 10^6$ N m s^{-1}. Whereas the short rise time (<5 s) slip patch propagated above and below the base of the brittle zone, as delineated by the depth of the aftershocks (see Fig. 3c), the long rise time slip patch appears to be mostly confined below.

aftershock locations provides further evidences for the diversity of the crustal response even for moderate size faults.

REFERENCES

Anastasiadis, A.N. *et al.*, 1999. The Athens (Greece) Earthquake of September 7, 1999: Preliminary Report on Strong Motion Data and Structure Response, The Institute of Engineering Seismology and Earthquake Engineering (ITSAK), Thessaloniki, Greece (accessed 2003 July 9; http://www.itsak.gr/report.html).

Baumont, D., Courboulex, F., Scotti, O., Melis, N. & Stavrakakis, G., 2002. Slip distribution of the Mw 5.9, 1999 Athens earthquake inverted from regional seismological data, *Geophys. Res. Lett.,* **29**(15), doi:10.1029/2001GL014261.

Bürgmann, R., Kogan, M.G., Levin, V.E., Scholz, C.H., King, R.W. & G. Steblov, M., 2001. Rapid aseismic moment release following the 5 December, 1997 Kronotsky, Kamchatka, earthquake, *Geophys. Res. Lett.,* **28,** 1331–1334.

Bürgmann, R., Calais, E., Freed, A., Freymueller, J.T. & Hreinsdóttir, S., 2003. Mechanics of Postseismic Deformation Following the 2002, Mw = 7.9, Denali Fault Earthquake, *EOS, Trans. Am. geophys. Un.,* Fall Meet. Suppl., **84**(46), Abstract G21B-0270.

Ergintav, S., Bürgmann, R., McClusky, S., Cakmak, R., Reilinger, R.E., Lenk, O., Barka, A. & Özener, H., 2002. Postseismic deformation near the Izmit earthquake (17 August 1999, M 7.5) rupture zone, *Bull. seism. Soc. Am.,* **92,** 194–207.

Fialko, Y., Sandwell, D., Agnew, D., Simons, M., Shearer, P. & Minster, B., 2002. Deformation on nearby faults induced by the 1999 Hector mine earthquake, *Science,* **297,** 1858–1862.

Harvard CMT Catalog, On-line Catalog, available at http://www.seismology.harvard.edu/CMTsearch.html.

Herrmann, R.B., 2002. *Computer programs in seismology. Volume III: An overview of synthetic seismogram computation*, Saint Louis university, Missouri.

International Seismological Centre, 2001. *On-line Bulletin* International Seismological Centre, Thatcham, UK, available at http://www.isc.ac.uk/Bull.

Julià, J., Ammon, C.J., Herrmann, R.B. & Correig, A.M., 2000. Joint inversion of receiver function and surface wave dispersion observations., *Geophys. J. Int.,* **143,** 99–112.

Kontoes, C., Elias, P., Sykioti, O., Briole, P., Remy, D., Sachpazi, M., Veis, G. & Kotsis, I., 2000. Displacement field and fault model for the September 7, 1999 Athens earthquake inferred from ERS2 satellite radar interferometry, *Geophys. Res. Lett.,* **27**(24), 3989–3992.

Louvari, E. & Kiratzi, A., 2001. Source parameters of the 7 September 1999 Athens (Greece) earthquake based on teleseismic data, *J. Balkan Geophys. Soc.,* **4**(3), 51–60.

Menke, W., 1984. *Geophysical data analysis: Discrete inverse theory*, Academic Press, Inc., Orlando.

Okada, Y., 1992. Internal deformation due to shear and tensile faults in a half-space, *Bull. seism. Soc. Am.,* **82**(2), 1018–1040.

Papadimitriou, P, Kaviris, G., Voulgaris, N., Kassaras, I., Delibasis, N. & Makropoulos, K., 2000. The September 7, 1999 Athens earthquake sequence recorded by the Cornet Network: preliminary results of source parameters determination of the mainshock, *Annales Geologiques des Pays Helleniques, 1e Serie,* **T. XXXVIII, Fasc. B.,** 29–35.

Papadimitriou, P, Voulgaris, N., Kassaras, I., Kaviris, G., Delibasis, N. & Makropoulos, K., 2002. The Mw = 6.0, 7 September 1999 Athens earthquake, *Natural Hazards,* **27,** 15–33.

Papadopoulos, G.A., Drakatos, G., Papanastassiou, D., Kalogeras, I. & Stavrakakis, G., 2000. Preliminary results about the catastrophic earthquake of 7 September 1999 in Athens, Greece, *Seism. Res. Lett.,* **71**(3), 318–329.

Pavlides, S.B., Papadopoulos, G. & Ganas, A., 2002. The fault that caused the Athens September 1999 Ms = 5.9 earthquake: Field observations, *Natural Hazards,* **27,** 61–84.

Pujol, J., 1988. Comments on the joint determination of hypocenters and station corrections, *Bull. seism. Soc. Am.,* **78,** 1179–1189.

Roumelioti, Z., Dreger, D., Kiratzi, A. & Theodoulis, N., 2003. Slip distribution of the September 7, 1999 Athens earthquake inferred from an empirical Green's function study., *Bull. seism. Soc. Am.,* **93**(2), 775–782.

Ruegg, J.C., Olcay, M. & Lazo, D., 2001. Co-, post- and pre (?)-seismic displacements associated with the Mw 8.4 southern Peru earthquake of 23 June 2001 from continuous GPS measurements, *Seism. Res. Lett.,* **72**(6), 673–678.

Sargeant, S.L., Burton, P.W., Douglas, A. & Evans, J.R., 2002. The source mechanism of the Athens earthquake, September 7, 1999, estimated from P seismograms recorded at long range, *Natural Hazards,* **27,** 35–45.

Stavrakakis, G.N., Chouliaras, G. & Panopoulou, G., 2002. Seismic source parameters for the Ml = 5.4 Athens earthquake (7 September 1999) from a new telemetric broad band seismological Network in Greece, *Natural Hazards,* **27,** 47–60.

Tselentis, G.-A. & Zahradnik, J., 2000a. Aftershock monitoring of the Athens earthquake of 7 September 1999, *Seism. Res. Lett.,* **71**(3), 330–337.

Tselentis, G.-A. & Zahradnik, J., 2000b. the Athens earthquake of 7 September 1999, *Bull. seism. Soc. Am.,* **90**(5), 1143–1160.

U.S Geological Survey, National Earthquake Information Center (USGS-NEIC), On-line Catalog, available at http://neic.usgs.gov/neis/sopar.

Voulgaris, N., Kassaras, I., Papadimitriou, P. & Delibasis, N., 2000. Preliminary results of the Athens September 7, 1999 aftershock sequence, *Annales Geologiques des Pays Helleniques, 1e Serie,* **T. XXXVIII, Fasc. B.,** 51–62.

Yagi, Y., Kikuchi, M. & Sagiya, T., 2001. Co-seismic slip, post-seismic slip, and aftershocks associated with two large earthquakes in 1996 in Hyuganada, Japan, *Earth Planets Space,* **53,** 793–803.

Zahradnik, J., 2002. *Focal mechanism of the Athens 1999 earthquake by ASPO method*, Research report, Department of Geophysics, Charles University, Prague.